Examining the performance of radio methods for determining the depth of air shower maximum in inclined cosmic ray simulations.

Anthony[1,2], Harm [1,2], Charles[1,2]

[1] IMAPP, Radboud University Nijmegen, Nijmegen, The Netherlands
[2] Nationaal Instituut voor Kernfysica en Hoge Energie Fysica (NIKHEF), Science Park, Amsterdam, The Netherlands

Abstract The study of Ultra-High-Energy Cosmic Rays (UHECR) relies on the detection of Extensive air showers. These Air Showers provide information on the primary particle type, energy, and incoming direction. Depending on the zenith angle, these EAS can be termed vertical ($\theta_z < 60°$) or inclined ($\theta_z \geq 60°$). Inclined air showers are of great interest to sparse radio UHECR detectors, such as the radio array that is part of the upgrade of the Pierre Auger Observatory and the future Giant Radio Array for Neutrino Detection (GRAND). At these zenith angles, the radio footprint becomes large enough that radio detection becomes feasible for sparse arrays i.e., antenna spacing $\gtrsim$ 1 km. The Cherenkov radius is a measure for the size of the radio footprint, which provides information on the depth of shower maximum (X_{max}) of EAS. However, this relation between the Cherenkov radius and shower depth is not trivial, especially for inclined showers. In this paper, we ...

Inclined air showers, Auger, GRAND, footprint, interferometry.

1 Introduction

Since the pioneering experiment in the 1960s [1], radio detection of ultra-high-energy cosmic rays experienced a period of dormancy, but in the last two decades, it has grown in prominence, becoming a significant technique in the field. The detection of the radio emission produced by Extensive air showers (EAS), hereafter referred to as radio detection, can be used to estimate properties of cosmic ray's primary energy, direction, and the depth of shower maximum (X_{max}) [2]. Determining X_{max} is an important task in astroparticle physics, as it constrains the mass of the primary particle and the nature of the particles' interactions within the atmosphere. Currently, fluorescence detection is the most reliable method for determining X_{max}. However, this method suffers from reduced statistics due to its inherent 15% duty cycle. Thus, an alternative method with a higher duty cycle that can provide comparable resolution on the shower depth would be advantageous. Radio signals produced by EAS are primarily emitted through geomagnetic and Askaryan mechanisms. The geomagnetic mechanism occurs due to the magnetic deflection of charged particles in the shower as they travel through the Earth's magnetic field. The Askaryan mechanism is a result of the drift of charge carriers in the shower as they propagate through the atmosphere [3]. Radio detection of EAS relies on the size and shape of the illuminated area on the ground, which is created by the interference of these two emission mechanisms, known as the radio footprint. This footprint includes a region of maximum coherence called the Cherenkov ring, which is characterised by an enhanced signal due to relativistic time compression resulting from the non-unity refractive index of the atmosphere [4]. The atmospheric depth of the source of radio emission, and the zenith angle determine the size of the radius of the Cherenkov ring, which scales to the size of the overall footprint.

The size of a radio footprint is primarily determined by two factors: the atmospheric depth of the emitter and the zenith angle. Shallow showers illuminate larger footprint areas than deeper ones because a diverging beam illuminates a smaller area as it penetrates deeper into the atmosphere. An increase in the zenith angle leads to exponential growth in the area of the footprint due to projection effects. This makes compact arrays like LOFAR more effective at detecting vertical showers as the

footprints cover small areas, while sparse arrays such as Auger and GRAND are sensitive to inclined showers due to their larger footprints [7]. However, the dependence of the radio footprint on the zenith angle and the X_{max} may change for highly inclined showers because they traverse through less dense atmosphere compared to vertical showers.

Prior studies have demonstrated the use of the footprint for X_{max} estimation [5], primarily focusing on vertical showers in both simulation and experimental data [6]. The two main distributions for estimating X_{max} are the amplitude of the geomagnetic emission and the spectral index distribution. The lateral distribution of amplitudes provides a measure of the Cherenkov radius and the overall size of the radio footprint, while the distribution of the spectral index uses the pulse shape obtained from the frequency domain of the radio signal [9].

In this paper, we explore the characteristics of the radio footprint of highly inclined air showers as a function of X_{max}. This understanding is crucial for future radio detectors as they will operate in this inclined shower regime. Our study is structured as follows: In Section 2, we investigate the features of the radio footprint as a function of the zenith angle and atmospheric depth of the source of radio emission. We use a model of the atmospheric refractive index to derive these characteristics. Section 2.1 confirms these findings through full-air shower simulations. We then analyse the X_{max} dependencies of the amplitude and spectral index distributions in Sections 4 and 5, respectively. Finally, in Section 6, we examine the performance of radio interferometry under different timing uncertainties at high zenith angles. We conclude the paper with a discussion in Section 7 and a summary of our main findings in Section 8.

2 Calculations based on atmospheric refractive index model

We employed the U.S. standard atmosphere [?] to model the relation between the zenith angle, footprint, and atmospheric depth of the radio emission. Here, the atmospheric depth refers to the slant depth (X), which is defined as a line integral of atmospheric density over the path length from infinity to a given point in the atmosphere. Using Eq. 1, we calculated the Cherenkov angle (ψ_C) based on the refractive index at a specific height ($n(z)$) in the atmosphere for a given zenith angle. By projecting the ψ_C onto the ground, we determined the Cherenkov radius (r_C) in a plane perpendicular

to the direction of propagation of the radio wavefront.

$$r_C = d\tan(\psi_C) = d\tan\left(\cos^{-1}\left(\frac{1}{\beta n(z)}\right)\right) \quad (1)$$

Here d is the geometrical distance from the ground to the radio emitter, $\beta \approx 1$ for an emitter moving at light speed. We used the atmospheric refractive index n as parametrised in ZHAires [10], which is given as an exponential function of altitude z, $n = 1 + ae^{-bz}$, where $a = 325 \times 10^{-6}$ and $b = 0.1218$ km^{-1}. Figure 2 shows r_C, calculated at a ground altitude of 1425 m, corresponding to the ground altitude of the Pierre Auger observatory, plotted as a function of the atmospheric depth of the radio emission for varying zenith angles θ.
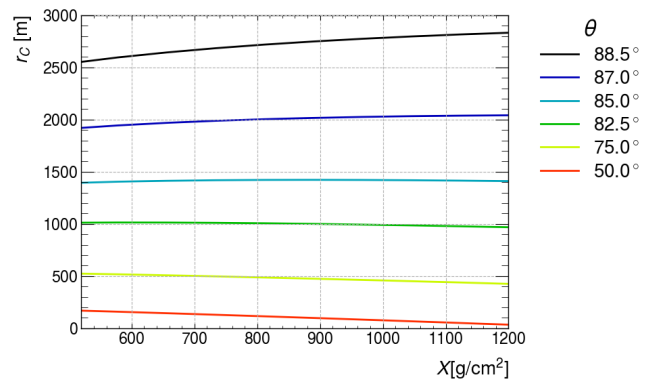

Fig. 1: The Cherenkov radius (r_C) as a function of slant depth (X) for different zenith angles (θ).

The results displayed in Fig. 2 indicate a consistent decrease in r_C as X increases for θ less than $82°$. For θ between $82.5°$ and $86°$, a single value of r_C can have two values of X. This θ region is also characterised by having a very minimal change in the value of r_C from a change in X. In the case of θ greater than $86°$, the footprint continuously increases as a function of X. However, the rate of increase changes from shallow to deep slant depths; i.e., the increase in the r_C range from 650 g/cm^2 to 700 g/cm^2 will be much larger than the change from 850 g/cm^2 to 900 g/cm^2 as can be seen in Fig. .

2.1 Impact of deviations in atmospheric depth on r_C and θ

To investigate the impact of deviations in the measured slant depth X on r_C and θ, we focused on a single depth of 750 g/cm^2, which is close to the average X_{max} recorded for showers above 10^{19} EeV by

the Pierre Auger Collaboration [**?**]. We introduced deviations of $\pm 10\,\mathrm{g/cm^2}$, $\pm 30\,\mathrm{g/cm^2}$, $\pm 50\,\mathrm{g/cm^2}$, and $\pm 100\,\mathrm{g/cm^2}$ as a proxy for uncertainties in the slant depth measurement. We then calculated the corresponding deviation in r_C, denoted by Δ_r, by working backwards from the deviations in X. Δ_r is given by:

$$\Delta_r(X, \Delta_X) = \frac{|(r(X + \Delta_X) - r(X)) + (r(X) - r(X - \Delta_X))|}{2} \quad (2)$$

And zenith angle deviation, $\pm \Delta_\theta$ given by:

$$\pm \Delta_\theta = |\theta(r_{750} \pm \Delta_r) - \theta(r_{750})| \quad (3)$$

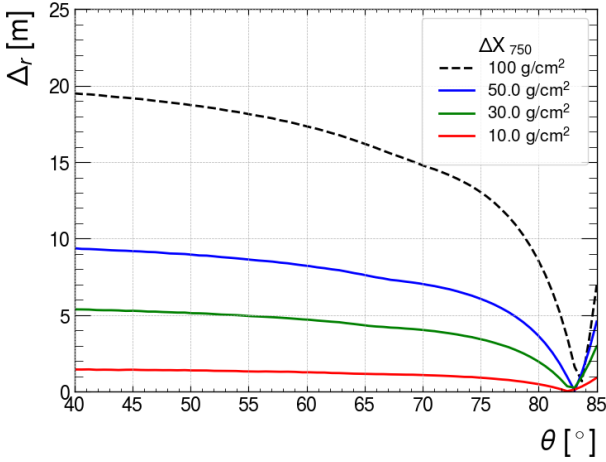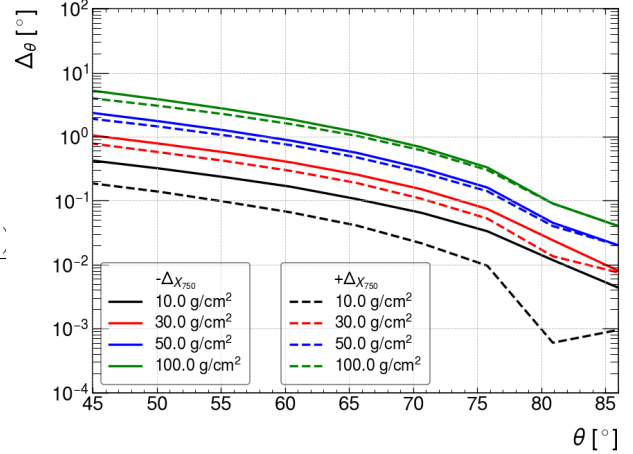This is shown graphically in Fig.2 and Fig. 3.

Fig. 3: Deviations on zenith angle (Δ_θ) as a function of zenith angle (θ) for different deviations on $X = 750\,\mathrm{g/cm^2}$.

Fig. 2: Deviations on the cherenkov radius (Δ_r) as a function of Zenith angle (θ) for different deviations on $X = 750\,\mathrm{g/cm^2}$.

Figure 2 and 3 show the deviations or resolution required on r_C and θ respectively, to attain a $\pm 10\,\mathrm{g/cm^2}$, $\pm 30\,\mathrm{g/cm^2}$, $\pm 50\,\mathrm{g/cm^2}$ and $\pm 100\,\mathrm{g/cm^2}$ deviation on an X of $750\,\mathrm{g/cm^2}$. The dips in Figure 2 between $82.5°$ and $84°$, indicate a minimal change in r_C at that value of θ despite changes in X. The figures can also be interpreted as; to achieve a resolution of $\pm 10\,\mathrm{g/cm^2}$, we would require a resolution of r_C of $\pm 2\,\mathrm{m}$ for $\theta \leq 75°$. We also observe a steepening in slope between $75°$ and $\approx 82°$. This shows how strong the zenith dependence is on the footprint in this zenith region. Figure 3, shows the asymmetry in Δ_θ, $+\Delta_{X_{750}}$ and $-\Delta_{X_{750}}$ shows how strong the r_C dependence is with increasing θ, as much smaller angles are required are to give the same change in r_C for the $+\Delta_{X_{750}}$ case as opposed to the $-\Delta_{X_{750}}$. We can also note that to archive a $\pm 10\,\mathrm{g/cm^2}$ on $750\,\mathrm{g/cm^2}$ would require a zenith angle accuracy of less

than a thousandth of a degree for zenith angles greater than $80°$. For a Δ_θ of $\pm 100\,\mathrm{g/cm^2}$, this is less than a tenth of a degree in zenith angle reconstruction for zenith angles greater than $80°$.

2.2 A Special Angle

In Fig. 2, shows a zenith angle region where the size of r_C with respect to X remains nearly constant. After examining Fig.2, we have identified this zenith angle region to start from approximately $82.85°$ and end at $86°$ for a U.S. standard atmosphere and ground altitude of $1425\,\mathrm{m}$. The lack of change in r_C is due to projection effects resulting from the signal being generated at a far distance from the ground, resulting in stretched emission cones over longer distances in the atmosphere than would be possible for vertical zenith angles, this is illustrated in Fig. 4.

In Fig. 4, the increase in n increases the ψ_C increases with larger values of n, this causes the emission cones from deeper emitters (X_E) to be slightly wider than those from shallow emitters (X_E). When $\theta << \theta_M$, both emitters are located relatively close to the ground. As a result, the shallower emitter r_C than the deeper emitter. When $\theta = \theta_M$, both emitters have the same r_C. This occurs because the effect of the source distances balances out with the broadening effect of ψ_C. For $\theta >> \theta_M$, the broader beam emitted by the source and the increased distance from the ground cause the deeper emitter to cover a larger r_C than the shallower showers.
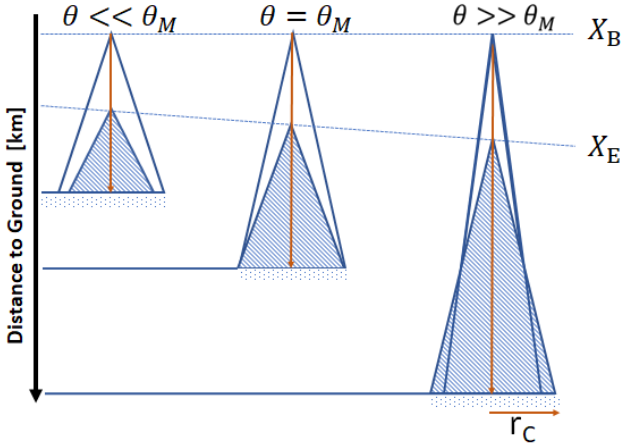
Fig. 4: The schematic illustrates the dependence of the Cherenkov radius (r_C) on the zenith angle (θ). We present three zenith angle scenarios; $\theta << \theta_M$, $\theta = \theta_M$, and $\theta >> \theta_M$. each with two emitters having the same difference in slant depth ($X_E - X_B$). The distance with respect to the zenith angle increases to cover the same difference in slant depth (X). For the case of θ_M, we found that r_C remains constant for both X_B and X_E.

3 Simulated air showers

To investigate if the findings in Sec.2 could be observed in radio Monte Carlo radio simulations. We generated 60 simulations using ZHAireS [10] version 1.0.30a. All simulations were composed of protons primaries with an energy of 1 EeV, and azimuth angle of $90\,^\circ$ in three discrete zenith angle bins i.e., $50\,^\circ$, $82.85\,^\circ$, and $88.5\,^\circ$. The corresponding r_C values for a shower with an X_{max} of $750\,\mathrm{g/cm^2}$ ($r_{C_{750}}$) to these zenith angles are $125\,\mathrm{m}$, $1053\,\mathrm{m}$ and $2690\,\mathrm{m}$, respectively. Each simulation contained 20 antennas evenly distributed along a length of $\approx 4\ r_{C_{750}}$ for that particular θ . The orientation of the antenna line was set perpendicular to the azimuthal direction of the incoming shower. We used a ground altitude of $1425\,\mathrm{m}$ and geomagnetic field parameters corresponding to the Pierre Auger observatory for all simulations, i.e., an Intensity of $23.57\,\mu\mathrm{T}$, a magnetic inclination of $-37.07\,^\circ$ and a declination of $0.52\,^\circ$. SIBYLL23d [11] was the hadronic model utilised and applied a relative thinning of 10^{-5}. From the 20 showers in each zenith angle set, 6 events were selected, these showers roughly covered an X_{max} range from $\approx 660\,\mathrm{g/cm^2}$ to $\approx 1050\,\mathrm{g/cm^2}$.

4 X_{max} dependence on the distribution of the Maximum Amplitudes

The lateral distribution of the maximum amplitude of the electric field against the antenna distance w.r.t. the shower core. This is a useful tool used in estimating r_C which can be used to determine X_{max} [6]. The point of maximum amplitude in the distribution corresponds to r_C given by Eq. 4. In Fig.5 We calculated the maximum amplitude in both the Pierre Auger observatory (30–80 MHz)[7] and GRAND (50–200 MHz)[?] frequency bands in the $\vec{v} \times \vec{B}$ polarisation, which corresponds to the polarisation direction from the geomagnetic emission of the shower. The effects of changing the band can be seen from the right (a,c,e) to left (b,d,f) plots in Figure 5. The narrow 30–80 MHz band gives much smoother distributions with amplitudes ≈ 3 times less than those of the broader 50–200 MHz band. The higher amplitudes in the 50–200 MHz band exhibited sharper features than those of the narrower band. This can be observed by the prominence of the plateau-like humps indicative of the Cherenkov ring, which can easily be distinguished up to an $X_{max} \approx 950\,\mathrm{g/cm^2}$ in image (b) in comparison to (a) of Figure 5.

Plots (a) and (b) in Fig. 5 demonstrate the X_{max} dependence from the distribution at a zenith angle of $50\,^\circ$. We observe that deeper and shallow showers have different shapes, and the width of the distribution increases with a reduction in X_{max} . This changes for very inclined showers, as depicted for the $88.5\,^\circ$ case, where shallower showers are seen to have narrower distributions than deep showers, with the shape of the distribution being identical. The amplitudes of the distributions in the $88.5\,^\circ$ are also greatly reduced owing to the signal traversing great distances through the atmosphere(i.e., $1/r$ dependence). The X_{max} ordering is present, but we expect added complexity to the signal brought about by a change in the radio emission mechanisms for showers developing in a less dense atmosphere [?]. At $82.85\,^\circ$, there is no discernable ordering of X_{max} as the width and general shape of the distributions are roughly the same, as depicted in images (c) and (d). All three cases agree with the scenarios sketched in Fig. 4.

5 X_{max} dependency of the spectral shape distribution

Figure 6 shows the frequency spectrum of different antennas w.r.t to the antenna distance to the shower core. As the distance from r_C increases, the slope of the frequency spectrum of the detected signal decreases. This change in slope is a result of the broadening of the pulse as a function of distance from the Cherenkov ring. At
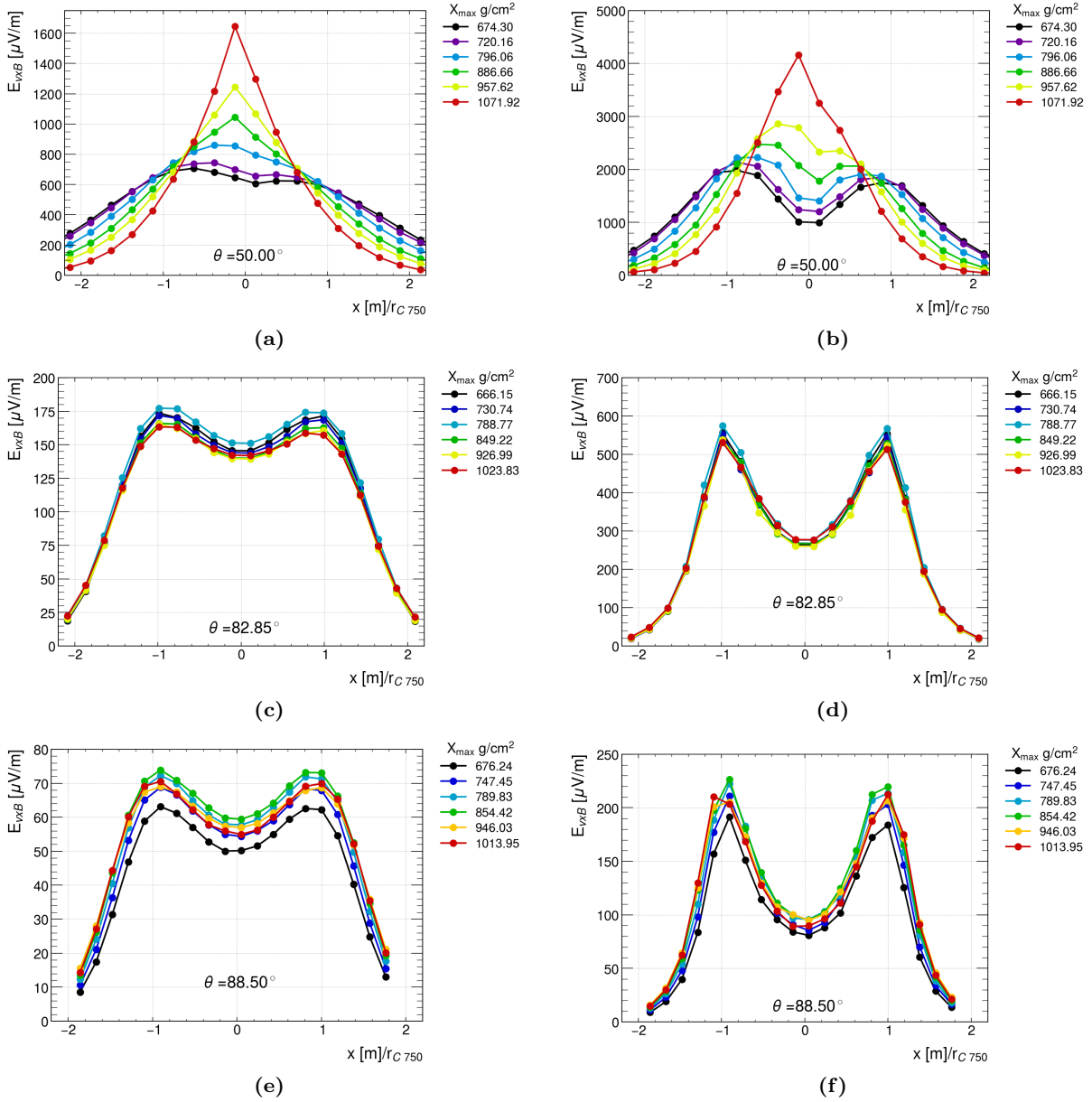
Fig. 5: Images (a,c,e); distribution of amplitudes in the frequency band 30 MHz–80 MHz. Images (b,d,f); the LDF in the 50 MHz–200 MHz frequency band for different X_{max}.

r_C , the fast pulse in the time-domain approaches a delta-function, resulting in a flat amplitude in the frequency domain, as illustrated in Fig.6. To determine the spectral index, we first determine the spectral slope by fitting a polynomial to the amplitude of the frequency domain, given by Eq. 4:

$$S(\nu - \nu_0) = a_1(\nu - \nu_0)^2 + a_2(\nu - \nu_0) + a_3 \qquad (4)$$

Here, S represents the amplitude of the signal as a function of frequency, with ν_0 denoting a reference frequency or slope frequency and the coefficients a_1, a_2,

and a_3 fit parameters. Evaluating the derivative of Eq.4 at ν_0 yields the spectral slope. To obtain the spectral index, we normalise the evaluated slope by the spectral amplitude at the slope frequency, as shown in Eq. 5.

$$b := \frac{1}{\ln(10) \cdot S(\nu - \nu_0)} \left(\frac{d}{d\nu} S(\nu - \nu_0) \right) \Big|_{\nu_0} = \frac{a_2}{\ln(10) \cdot a_3}$$
$$(5)$$

$S(\nu - \nu_0)$ represents any well-fitting function to the frequency domain, given by Eq. 4 in our case, and ν_0 is the slope frequency. This formulation of the spectral in-
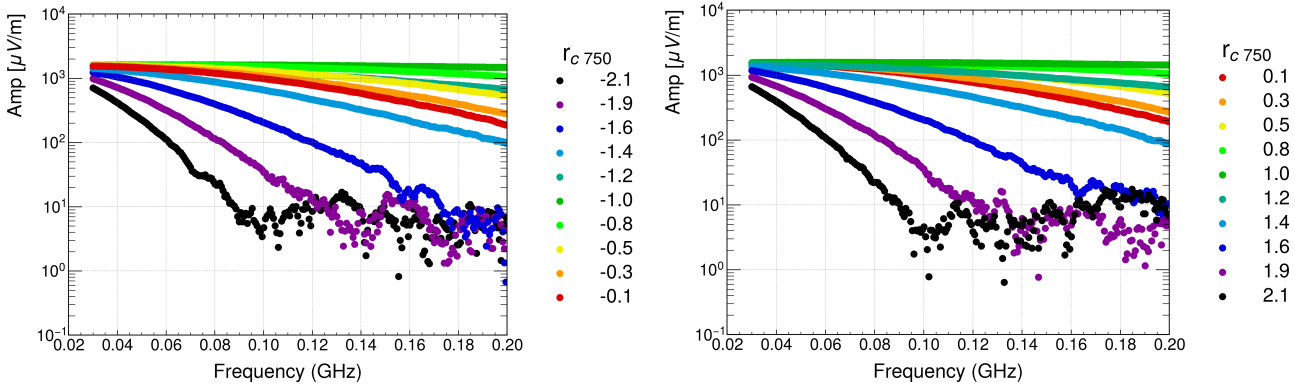
Fig. 6: The frequency spectrum as a function of antenna distance from shower core.

dex is equivalent to previous analyses that obtained the spectral index as one of the coefficients of the fit equation: $S(\nu - \nu_0) = 10^{b(\nu - \nu_0) + c}$ to the frequency spectrum [?]. The spectral index b characterises the pulse shape, reducing signal amplitude dependence. Figure 7 shows the distributions of the spectral index as a function of antenna distance to the shower core obtained at $\nu_0 = 50\,\text{MHz}$ and $\nu_0 = 150\,\text{MHz}$. To get rid of antennas with thinning artefacts in our analysis, we applied a filter to remove antennas with low signal, which was determined by a threshold equal to 5 times the median value of the amplitudes for frequencies greater than 100 MHz of the two antennas located at the edges of the antenna line. In Fig.7, we observe that the lower slope frequency gives a much smoother distribution with a very clear X_{max} dependence. The spectral index for $\nu_0 = 50\,\text{MHz}$ shows X_{max} ordering at distances $\geq 1\ r_C$ for the $50°$ and $88.5°$ cases, with the notable difference being the inversion of the X_{max} ordering. This is similar to our observations in the distribution of amplitudes and slopes. The higher slope frequency has very prominent bumps at r_C but the distributions have no discernable X_{max} dependency, especially for the inclined cases. For the $82.85°$ case, the ordering in X_{max} starts at around $1.5\,r_C$ with no visible fluctuations at r_C.

In both the distribution of maximum amplitudes and spectral indices, the X_{max} dependency of the two distributions can be seen to invert from low to high zenith angles. However, both distributions do not give any discernable change on the r_C as a function of X_{max} at $82.85°$. Thus, X_{max} measurements done in the $82° - 86°$ range would require an alternative method.

6 X_{max} Dependency from interferometry

To evaluate the potential of interferometry in resolving the X_{max} in the region where the amplitude distribu-

tion and spectral slopes had minimal sensitivity i.e., at a zenith angle of $82.85°$, we created a second set of simulations to be used for the Radio Interferometric Technique (RIT) [12]. The simulation set consisted of 160 antennas arranged on a hexagonal grid with a spacing of $1.5\,\text{km}$ and another set at $1\,\text{km}$ to resemble the Pierre Auger Observatory's and GRAND setups, respectively. All other inputs for the simulations remained similar to the simulation set discussed in Sec. 3.

The RIT technique has been demonstrated to reconstruct the direction and X_{max} by utilizing coherent sums of the radio signals arriving at different antennas in the array. The use of interferometry in sparse array setups is especially possible at high zenith angles because the radio footprints become large enough to cover a sufficient number of baselines. Figure 8 shows the normalised integrated power in the transverse plane of the shower, the longitudinal integrated power as a function of slant depth X and the correlation plot of the RIT reconstructed X_{max} against the simulated X_{max}. The reconstruction in these plots assumes ideal synchronisation, i.e., having zero timing uncertainties between antennas.

To investigate how timing uncertainties affect the performance of X_{max} reconstruction, we added different levels of Gaussian timing uncertainties to the time traces of the simulations and performed the reconstruction. The results in Fig. 9 show $\sigma_{X_{\text{max}}}$ calculated as Root-mean-square (RMS) of the reconstructed X_{max} (X_{rit}) values plotted against the timing uncertainty σ_t.

As shown in Fig. 9, for timing uncertainties within $5\,\text{ns}$, there is a notable linear correlation between X_{rit} and the simulated X_{max}. However, beyond $5\,\text{ns}$ of timing jitter, the accuracy of the reconstruction quickly diminishes as you lose coherency. This lack of coherency above a quarter wavelength. It is worth emphasizing that the RMS logarithmically scales with the timing uncertainty. This logarithmic scaling signifies that higher
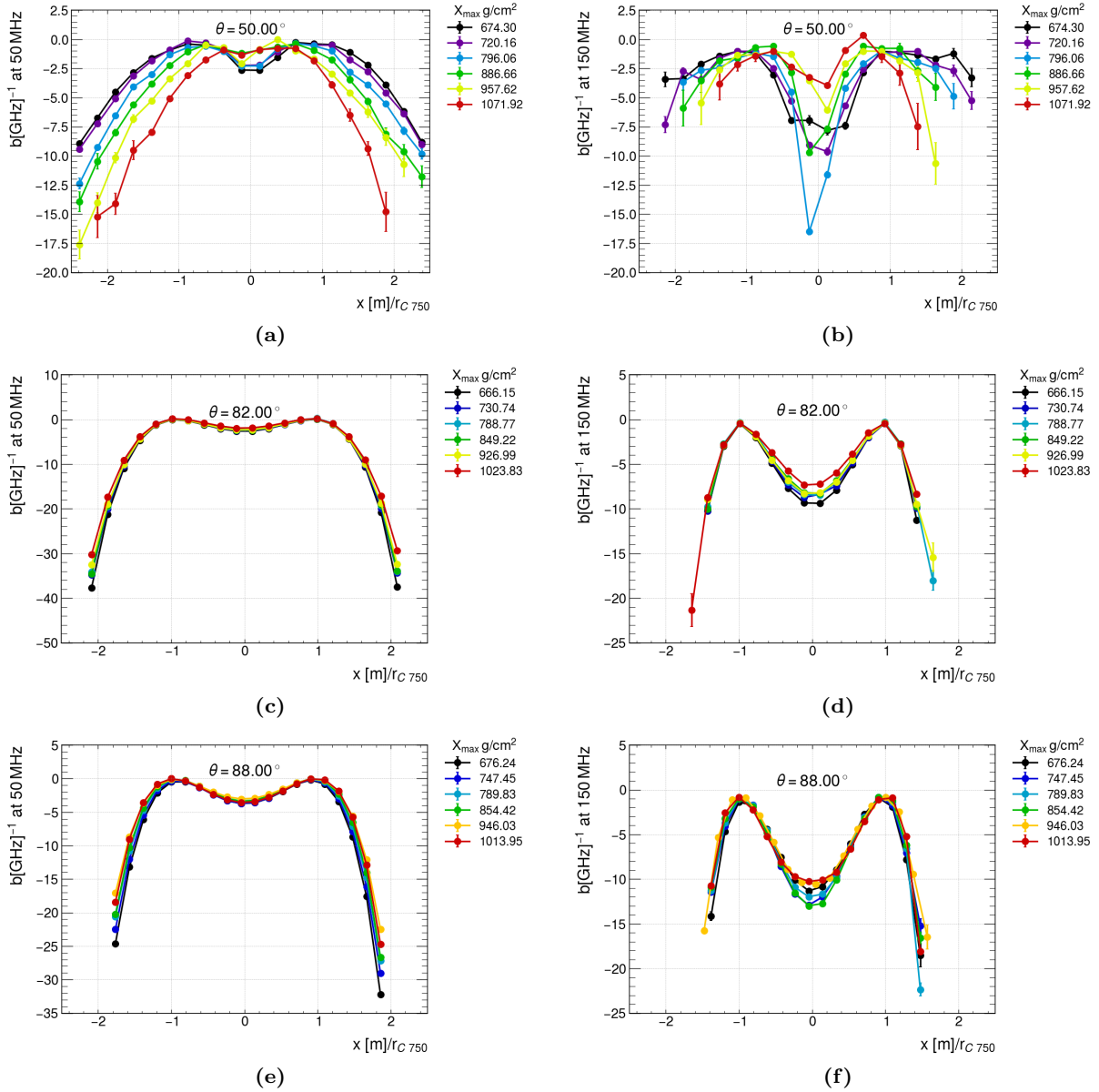
Fig. 7: The spectral index distribution for varying X_{max} at slope frequencies of 50 MHz (a,c,e) and 150MHz (b,d,f).

levels of timing uncertainty exert a more substantial influence on the accuracy of the X_{rit} .

7 Discussion

In sections 4 and 5 we demonstrated the use of the r_C as a measurement for the maximum shower depth. However, we have also identified limitations of methods reliant on r_C and the radio footprint in general. Specifically, in sparse array setups, to achieve a $\pm 10\,\mathrm{g/cm^2}$ resolution on shower maximum requires a resolution of ± 2 m on r_C and angular resolution of $\pm 0.001\,^\circ$ for zenith angles greater than $80\,^\circ$. Both these values are beyond the accuracies currently attainable for sparse setups.

As demonstrated, both the LDF of the amplitudes and the slope distribution have sensitivity for estimating X_{max} at $\theta < 82°$ and $> 86°$. But in the region $82\,^\circ < \theta < 86\,^\circ$, both these methods lose sensitivity to shower depth, as the dependence of r_C on shower depth transitions from flat to parabolic.

However, using interferometry, the size of the r_C only helps cover baselines that are later used in the coherent sum. For which, even at the extreme case of $82.85\,^\circ$, the number of baselines is adequate for high-precision measurements of X_{max} even with several nanoseconds of jitter. It's also worth noting that the addition
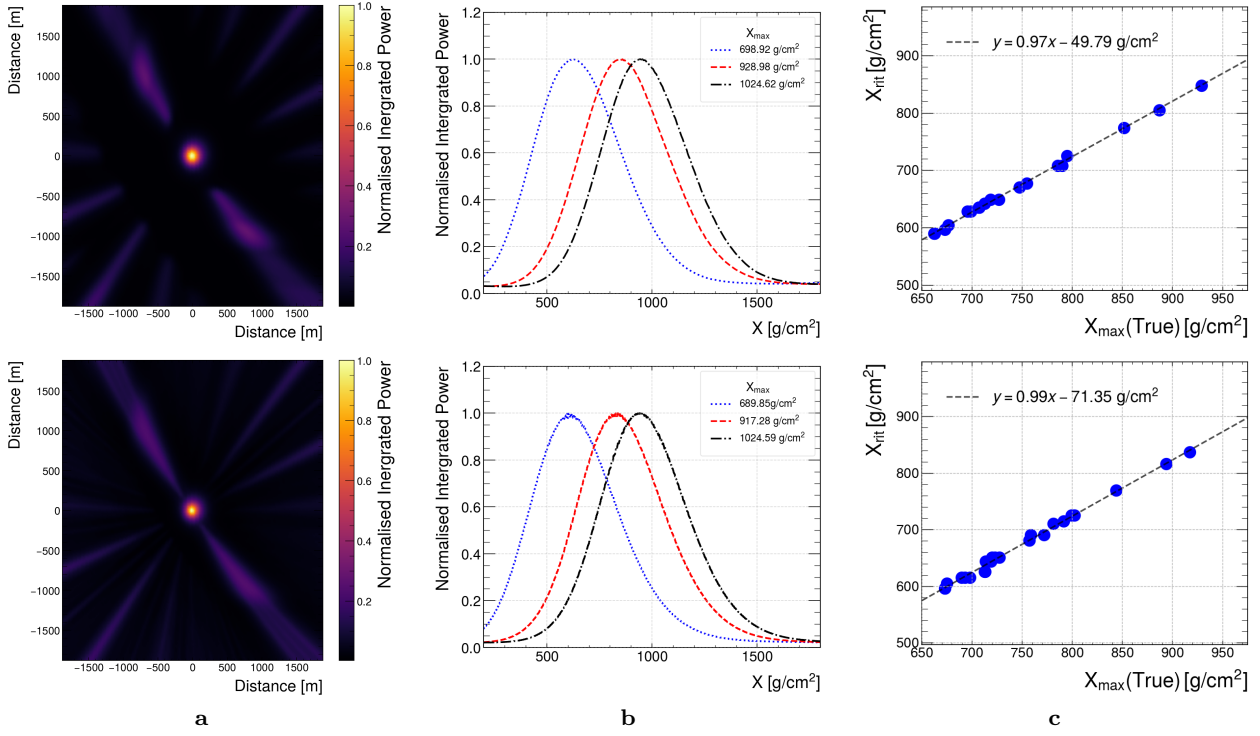
Fig. 8: (a) A transverse slice of the atmosphere showing the integrated power at an atmospheric depth of $750\,\text{g/cm}^2$ in the shower plane. (b) A plot illustrates the normalized power against the slant depth X for three simulated showers. The power in images (a) and (b) is normalised by the maximum power. (c) A correlation plot comparing the true X_{max} with the RIT reconstructed X_{max} (X_{rit}) at a zenith angle of 82.85 degrees. The reconstruction was performed without any timing jitter or noise. The top images correspond to the frequency range of 30-80 MHz with an antenna spacing of 1500 m, while the bottom images correspond to the frequency range of 30-200 MHz with an antenna spacing of 1000 m.
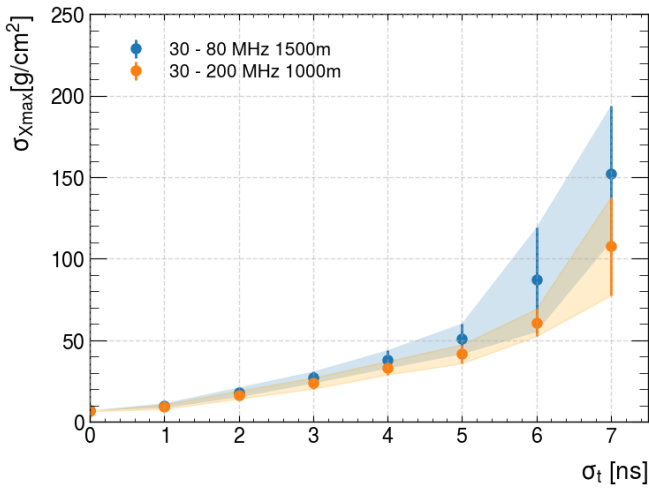

Fig. 9: Uncertainties in X_{max} ($\sigma_{X_{\text{max}}}$) as a function of the timing uncertainty σ_t.

of jitter to interferometric reconstruction reduces the resolution on the depth shower maximum from $\approx \pm$

$5\,\text{g/cm}^2$ for sub-nanosecond jitter, to $\approx \pm\,100\,\text{g/cm}^2$ for $\approx 6\,\text{ns}$ jitter. Above this level of jitter, the method loses coherency in the signal and can reconstruct neither the direction nor the shower depth, as shown in Fig.9. The combination of jitter, noise, and trigger thresholds is left for future studies.

The constant values of r_C and the footprint at the "magic angle" can provide an effective scaling of the electromagnetic energy to the particle energy, which will be useful in the calibration of the energy reconstruction of radio arrays.

A significant limitation of the radio interferometric technique is that, for an antenna spacing of $\approx 1\,\text{/km}$, the reconstruction may only be applicable for zenith angles above $70°$, as lower zenith angles reduce the number of baselines. This could be complemented by incorporating other techniques, such as the slope method, to improve the measurement of X_{max}.

8 Conclusion

Overall, the study shows the methods and limitations of utilizing the r_C to infer the shower maximum for inclined air showers. However, utilizing the radio interferometric technique would greatly enhance sparse arrays' mass detection sensitivity and capacity. On the other hand, how well this method performs will be subject to the accuracy of the timing synchronisation.

References

1. H.R. ALLAN, J.K. JONES, Nature **212**, 129 (1966). DOI 10.1038/212129a0
2. T. Huege, **44**, 520 (2014). DOI 10.1007/s13538-014-0226-6
3. J. Alvarez-Muñiz, W.R. Carvalho, H. Schoorlemmer, E. Zas, Astroparticle Physics **59**, 29 (2014). DOI https://doi.org/10.1016/j.astropartphys.2014.04.004
4. K.D. de Vries, A.M. van den Berg, O. Scholten, K. Werner, Phys. Rev. Lett.**107**(6), 061101 (2011). DOI 10.1103/PhysRevLett.107.061101
5. K.D. de Vries, O. Scholten, K. Werner, Astroparticle Physics **45**, 23 (2013). DOI https://doi.org/10.1016/j.astropartphys.2013.02.003. URL https://www.sciencedirect.com/science/article/pii/S0927650513000297
6. S. Buitink, A. Corstanje, H. Falcke, J.R. Hörandel, T. Huege, A. Nelles, J.P. Rachen, L. Rossetto, P. Schellart, O. Scholten, S. ter Veen, S. Thoudam, T.N.G. Trinh (et al), Nature **531**(7592), 70 (2016). DOI 10.1038/nature16976. URL https://doi.org/10.1038/nature16976
7. A. Aab et al, J. Cosmology Astropart. Phys.**2018**(10), 026 (2018). DOI 10.1088/1475-7516/2018/10/026
8. F. Schlüter, T. Huege, Journal of Cosmology and Astroparticle Physics **2023**(01), 008 (2023). DOI 10.1088/1475-7516/2023/01/008. URL https://dx.doi.org/10.1088/1475-7516/2023/01/008
9. S. Grebe, P.A. Collaboration, (2013). DOI 10.1063/1.4807524
10. J. Alvarez-Muniz, W. Carvalho Jr., E. Zas, Astroparticle Physics **35**(6), 325 (2012). DOI 10.1016/j.astropartphys.2011.10.005
11. F. Riehn, R. Engel, A. Fedynitch, T.K. Gaisser, T. Stanev, Phys. Rev. D **102**, 063002 (2020). DOI 10.1103/PhysRevD.102.063002. URL https://link.aps.org/doi/10.1103/PhysRevD.102.063002
12. H. Schoorlemmer, W.R. Carvalho, The European Physical Journal C **81**(12) (2021). DOI 10.1140/epjc/s10052-021-09925-9